nanomaterials

MDPI

Article

GABr Post-Treatment for High-Performance $MAPbI_3$ Solar Cells on Rigid Glass and Flexible Substrate

Tingting Chen [1], Rui He [1], Fan Zhang [2], Xia Hao [2,3,*], Zhipeng Xuan [2], Yunfan Wang [2], Wenwu Wang [1,3], Dewei Zhao [1,3], Jingquan Zhang [1,3] and Lili Wu [1,3,*]

1 College of Materials Science and Engineering, Sichuan University, Chengdu 610065, China; chentingting1@stu.scu.edu.cn (T.C.); hrkbjj@stu.scu.edu.cn (R.H.); www1492@scu.edu.cn (W.W.); dewei.zhao@scu.edu.cn (D.Z.); zhangjq@scu.edu.cn (J.Z.)
2 Institute of New Energy and Low-Carbon Technology, Sichuan University, Chengdu 610065, China; zhangfan3@stu.scu.edu.cn (F.Z.); 2018226220003@stu.scu.edu.cn (Z.X.); wangyunfan@stu.scu.edu.cn (Y.W.)
3 Engineering Research Center of Alternative Energy Materials & Devices, Ministry of Education, Chengdu 610065, China
* Correspondence: hao.xia0808@scu.edu.cn (X.H.); wulili@scu.edu.cn (L.W.)

Abstract: Perovskite solar cells have exhibited astonishing photoelectric conversion efficiency and have shown a promising future owing to the tunable content and outstanding optoelectrical property of hybrid perovskite. However, the devices with planar architecture still suffer from huge V_{oc} loss and severe hysteresis effect. In this research, Guanidine hydrobromide (GABr) post-treatment is carried out to enhance the performance of $MAPbI_3$ n-i-p planar perovskite solar cells. The detailed characterization of perovskite suggests that GABr post-treatment results in a smoother absorber layer, an obvious reduction of trap states and optimized energy level alignment. By utilizing GABr post-treatment, the V_{oc} loss is reduced, and the hysteresis effect is alleviated effectively in $MAPbI_3$ solar cells. As a result, solar cells based on glass substrate with efficiency exceeding 20%, V_{oc} of 1.13 V and significantly mitigated hysteresis are fabricated successfully. Significantly, we also demonstrate the effectiveness of GABr post-treatment in flexible device, whose efficiency is enhanced from 15.77% to 17.57% mainly due to the elimination of V_{oc} loss.

Keywords: nonradiative recombination; post-treatment; flexible perovskite solar cell

Citation: Chen, T.; He, R.; Zhang, F.; Hao, X.; Xuan, Z.; Wang, Y.; Wang, W.; Zhao, D.; Zhang, J.; Wu, L. GABr Post-Treatment for High-Performance $MAPbI_3$ Solar Cells on Rigid Glass and Flexible Substrate. *Nanomaterials* **2021**, *11*, 750. https://doi.org/10.3390/nano11030750

Academic Editor: Jung-Ho Yun

Received: 1 February 2021
Accepted: 11 March 2021
Published: 16 March 2021

1. Introduction

Organic–inorganic hybrid perovskites have received great attention due to their superior properties of high light absorption coefficient [1], low exciton binding energy [2], and long diffusion length [3], which are suitable for application in photovoltaic devices. Lead-based organic perovskite ($APbX_3$, A = $CH_3NH_3^+$, $CH(NH_2)_2^+$, alkali metal ion or mixed cations; X = I, Cl, Br or mixed anions) is easy to fabricate and the power conversion efficiency (PCE) for the state-of-the-art device has achieved 25.5% [4]. Meanwhile, the stability obstacle is gradually being overcome after numerous efforts have been paid to it [5,6]. $MAPbI_3$ is the commonly used material in perovskite solar cell (PSCs) with lower Urbach Energy (~19 meV) than other photovoltaic materials and is relatively cheap to produce with simple composite [7]. The development of $MAPbI_3$-based PSCs is rapid, but the device performance still suffers from nonnegligible nonradiative recombination [8,9]. $MAPbI_3$ is compatible with various fabrication techniques, and among which the solution process is commonly taken in experiments due to the advantage of low temperature and easy operation. However, the film deposited through solution method is usually polycrystalline with high density of defects situated at the grain boundary or the film surface, which act as nonradiative recombination centers and result in serious efficiency loss [10–14]. Besides, the existence of defects will induce ion migration in perovskite layer and thus cause serious hysteresis in solar cells which brings difficulty in determining the accurate efficiency of PSCs [15,16].

Compositional engineering and surface modification are two main strategies to improve the performance of solar cells. Guanidinium cation (GA^+) is an effective defect passivator due to the unique hydrogen bonding capability [17]. In 2014, GASCN and $GANO_3$ were employed as additives in dye-sensitized solar cells to decrease the electron/iodine recombination and enhance the collection efficiency [18]. Yang et al. doped GAI into $MAPbI_3$ precursor directly and promoted the PCE to over 17%. They found out that the incorporation of GA could improve the film continuity without changing the crystal structure of perovskite [19]. Zhou et al. introduced GABr into $FA_{0.7}MA_{0.3}Pb_{0.7}Sn_{0.3}I_3$ perovskite and found that GABr could reduce the defects caused by the oxidation of Sn^{2+} and hence improve the PCE and stability performance [20]. Except for introducing GA^+ into perovskite composition, several studies employed GA salts treatment on perovskite layer and the performance optimization of devices were also observed [21–23]. Yan et al. developed $CsPbI_3$ PSCs through GABr treatment and they proposed that this treatment would induce ion exchange between I^- and Br^- and then cause the formation of 2D GA-$CsPbI_xBr_y$ to passivate defects [21]. In Chen's work, they applied a GABr solution to modify the wide-bandgap perovskite surface and demonstrated the formation of a graded perovskite homojunction which resulted in effective grain boundary passivation after treatment [22]. In Zhang's research, GABr post-treatment induced a 2D/3D heterostructure in $Cs_{(1-x)}Rb_xPbI_2Br$ perovskite and reduced the density of defects [23].

Except for energy loss caused by defects state, $MAPbI_3$ n-i-p planar solar cell suffers from a severe hysteresis effect. The rapid nucleation and grain growth might be the main reasons for the formationof defective films and the hysteresis is suspected to be caused by defect induced ion migration, the fundamental properties of $MAPbI_3$, e.g., the dipole moment, and so on [24]. Therefore, GABr treatment on $MAPbI_3$ seems to be ideal in optimizing the device performance for the two reasons: (1) the nearly zero dipole moment of GA^+ is beneficial for adjusting the polarity for perovskite to reduce the hysteresis [25,26], (2) Br^- will compete with I^- in I-based perovskite and can retard the crystal process to achieve less-defective films [20,27]. However, the application of GABr post-treatment on $MAPbI_3$ PSCs with n-i-p planar structure has been rarely reported and it is worth exploring.

Thus, we attempt to utilize GABr post-treatment to modify the $MAPbI_3$ PSCs with n-i-p planar architecture. Notably, if the content of GABr is too high, the phase segregation might be induced [28] and the large GA cation will block the charge transfer which can result in poor device performance [29,30]. Therefore, special care should be taken while the GABr treatment is carried out.

Among the lead-based organic perovskites, $MAPbI_3$-based planar PSCs is one especially appropriate architecture to develop flexible photovoltaic cell as the annealing temperature is compatible with the plastic substrates. It is well known that flexible cells have been rapidly developed due to their light weigh, excellent bending resistance, and suitablility for being employed in wearable electronics, flying objects, and smart textiles. However, the development of flexible PSCs still suffers from poor efficiency which is much lower than rigid PSCs. To the best of our knowledge, the state-of-the-art PCE of rigid $MAPbI_3$-based PSCs has reached 21.88% [31] and several works have been carried out to improve the efficiency of flexible PSCs to over 18% [8,32–34]. Considering that the low-temperature manufacturing of GABr treatment (<150 °C) and the previous applications in improving the device performance, it is expected to utilize this optimization method to improve the efficiency of flexible devices [21,22,35,36].

In this work, we conducted a simple GABr post-treatment and investigated the effects on $MAPbI_3$ films and solar cells. Thanks to the improved film quality, reduced defect states, and suppressed hysteresis, an optimized performance is demonstrated in both rigid and flexible $MAPbI_3$ based PSCs.

2. Materials and Methods

2.1. Materials

The indium tin oxide (ITO) glass substrate was purchased from Pilkington Group Limited, and the PEN-ITO substrate was purchased from Peccell (Kanagawa, Japan). Lead (II) iodide (PbI_2, 98%), Guanidine Hydrobromide (GABr, 98%) were purchased from TCI (Tokyo, Japan). SnO_2 colloid (15 wt%) was supplied by Alfa Aesar (Shanghai, China). N,N-dimethylformamide (DMF, >99%), dimethyl sulfoxide (DMSO, >99%), Isopropyl Alcohol (IPA, >99%), chlorobenzene (99%), Acetonitrile (>99%), (4-tert-Butylpyridine (tBP, >99%) and lithium-bis(trifluoromethanesulfonyl)imide (Li-TFSI, >99%) were purchased from Sigma-Aldrich (St. Louis, MO, USA). 2,2′,7,7′7-tetrakis-(N,N-di-p-methoxyphenylaminor)-9,9′-spiroobifluorene(Spiro-OMeTAD, >99.5%) and Methylamine Hydroiodide (MAI, 99.5%) were purchased from Xi'an polymer light Technology Crop (Xi'an, China).

2.2. Preparation of Devices

ITO coated glass substrates were cleaned by diluted detergent and rinsed with deionized water. Then, the substrates were cleaned by ultra-sonication with deionized water, alcohol for 15 min in sequence and dried by N_2 gas. After drying, the substrates were sent to an ultraviolet ozone chamber and treated for 15 min. SnO_2 precursor solution was prepared by mixing SnO_2 colloid and deionized water (volume ratio, 1:3). SnO_2 layer was spin-coated on the substrate at 4000 rpm for 20 s and then annealed at 160 °C for 20 min. After being cooling down, the ultraviolet-ozone treatment on SnO_2 was carried out and the duration was set as 15 min. In this study, $MAPbI_3$ is prepared by one-step spin-coating deposition method with anti-solvent and then GABr treatment is carried out and optimized by varying the concentrations of GABr in IPA. The perovskite precursor solution was prepared by dissolving 714.56 mg PbI_2 and 246.38 mg MAI (molar ratio, 1:1) in 1 mL DMF/DMSO (volume ratio, 9:1). The $MAPbI_3$ was spin-coated on SnO_2 at 4000 rpm for 25 s, and the antisolvent of 200 μL chlorobenzene was dripped at 10 s in the process in N_2-filled glove box. The as-prepared perovskite samples were sequentially annealed at 60 °C for 2 min and then 110 °C for 25 min. The GABr solutions were prepared by dissolving x mg GABr powder into 1 mL IPA corresponding to different concentrations. The GABr was then dropped on and spin-coated quickly at 4000 rpm for 30 s. Then the film was annealed at 105 °C for 5 min. Spiro-OMeTAD solution was prepared by dissolving 72.3 mg Spiro-OMeTAD, 17.5 mL Lithium salt solution (520 mg Li-TFSI in 1 mL Acetonitrile) and 28.75 mL tBP in 1 mL chlorobenzene. Spiro-OMeTAD was spin-coated at 3000 rpm for 30 s and then the samples were stored in a chamber filled with dried oxygen for 12 h. Afterward, Au electrode (~70 nm) was deposited by vacuum evaporation with a shadow mask.

As for the devices for SCLC test, the SnO_2 was substituted by PEDOT:PSS, and it was spin-coated on substrate at 5000 rpm for 30 s, and annealed at 150 °C for 15 min. Then, the substrates were sent to glove box directly for the next step without other treatment.

The flexible devices were prepared in the same way except for substrates cleaning and annealing process of SnO_2. The ITO coated PEN was used as received without cleaning. The SnO_2 was annealed at 110 °C for 50 min.

2.3. The Characterization of Films and Devices

The XRD patterns were obtained by an X-ray diffractometer (XRD, Shimadzu XRD-6100, Tokoy, Japan) with Cu-Kα (λ = 1.5405 Å) radiation source. The absorption spectra were obtained by Lambda 950 UV/Vis spectrophotometer (PerkinElmer Inc., Waltham, MA, USA). The surface and cross-sectional images were observed by field-emission scanning electron microscopy (FE-SEM, Regulus-8230, Hitachi, Tokyo, Japan). The AFM images and KPFM images were obtained by using an atomic force microscopy (DI Multimode 8, Bruker Nano Inc., Munich, Germany). PL and TRPL spectra were measured by FLS980 fluorescence spectrometer (Edinburgh Inc., Livingston, Scotland, UK). XPS and UPS spectra were measured by using a photoelectron spectrometer (ESCALAB 250Xi, Thermo Fisher Scientific, Waltham, MA, USA). The *J-V* measurements and SCLS tests were conducted by

using a Keithley 2634B source meter (Cleveland, OH, USA) under AM 1.5G illumination (100 mW cm^{-2}). The active area of cells was defined by a shadow mask as 0.0975 cm^2. The spectral response measurements were performed by a solar cell quantum efficiency measurement system (QEX10, PV Measurements, Inc., Boulder, CO, USA).

3. Results and Discussion

X-ray diffraction (XRD) is carried out to explore the impact of different concentrations of GABr on the crystal structure of $MAPbI_3$. Figure 1a shows the XRD patterns of perovskites treated with different concentrations of GABr. x GABr denotes x mg·ml^{-1} GABr treatment in this work unless otherwise noted. The diffraction peaks at 14.08°, 28.42° and 31.88° corresponding to the (110), (220), and (330) planes of $MAPbI_3$, and the peak at 12.78° is assigned to PbI_2, which disappears after GABr treatment [37,38]. The intensity of $MAPbI_3$ peaks gradually increases at low concentrations of GABr, whereas when x is higher than 5, the intensity decreases. When x = 8, two new diffraction peaks at 8.71° and 10.72° appear, and this indicates the formation of 2D GA_2PbI_4 [39]. Furthermore, GA^+ might locate at the grain boundary or the surface of the perovskite layer, rather than entering the lattice of $MAPbI_3$ because there is no obvious shift observed in $MAPbI_3$ peaks. Notably, with the increased concentration of GABr, the intensity of GA_2PbI_4 peaks increases while that of $MAPbI_3$ decreases. This suggests that an appropriate content of GABr will enhance the crystallinity of $MAPbI_3$, but excess GABr will disrupt the crystallinity and generate 2D GA_2PbI_4. Afterwards, we apply ultraviolet-visible (UV-vis) absorption spectroscopy to observe the alternation of optical properties of perovskite layers. The absorption spectra are shown in Figure 1b, and the absorption band edge shifts to short wavelength with the increased x. As $MAPbI_3$ is a direct-bandgap semiconductor, the optical bandgap can be calculated by Tauc relationship illustrated in Equation (1):

$$(\alpha h\nu)^2 = C\,(h\nu - E_g), \quad (1)$$

where α is absorption coefficient, h is Planck's constant, ν is frequency of vibration, and C is proportional constant. Then, we obtain the Tauc plot shown in Figure 1c, the optical bandgap (E_g) is calculated from the intersection between the cut-off edge and the x-axis. E_g becomes larger with the increasing concentration of GABr, revealing the incorporation of Br into $MAPbI_3$ lattice by partially replacing I site.

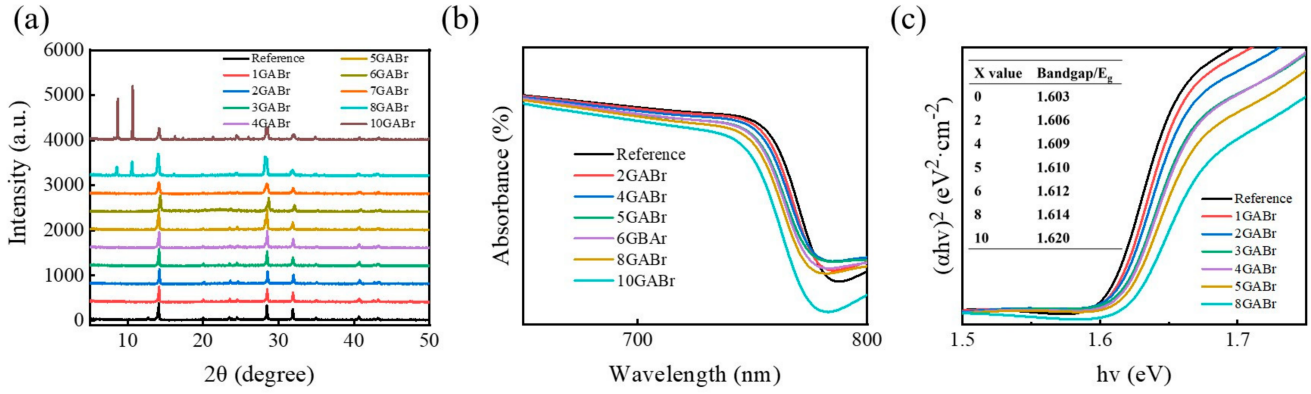

Figure 1. (**a**) XRD patterns of pristine $MAPbI_3$ and perovskite films, (**b**) the UV-vis absorption spectra, and (**c**) $(\alpha h\nu)^2$ versus energy of perovskite films, treated by GABr with different concentrations.

The current density-voltage (*J-V*) measurement is carried out to directly understand the influence of GABr post-treatment on the device performance. The typical *J-V* parameters including short circuit current density (J_{sc}), open circuit voltage (V_{oc}), fill factor (*FF*), and PCE are summarized and depicted in Figure 2a–d. The results indicate that the GABr treatment induces a significantly improvement of V_{oc} when x < 7, and slightly decrease

after x exceeds 7. J_{sc} and *FF* keep increasing as the concentration increases from 0 to 4, but when x $\geq$ 5, J_{sc} and *FF* drop severely. The devices achieve the best performance at x = 4 and give the highest V_{oc} = 1.148 V at x = 6. This indicates that moderate concentration of GABr can achieve an obvious promotion of device performance, while excess GABr will deteriorate the device performance. Herein, we denote 4 GABr as GABr in the following content, unless the special explanation. Then, we statistic the V_{oc} and PCE of devices without and with GABr treatment to evaluate the effect of GABr treatment (Figure 2e,f). The average V_{oc} of reference devices is 1.033 V, whereas the average V_{oc} of GABr-based devices is 1.108 V. The average PCE's are 16.2% and 19.2% for pristine devices and treated devices, respectively.

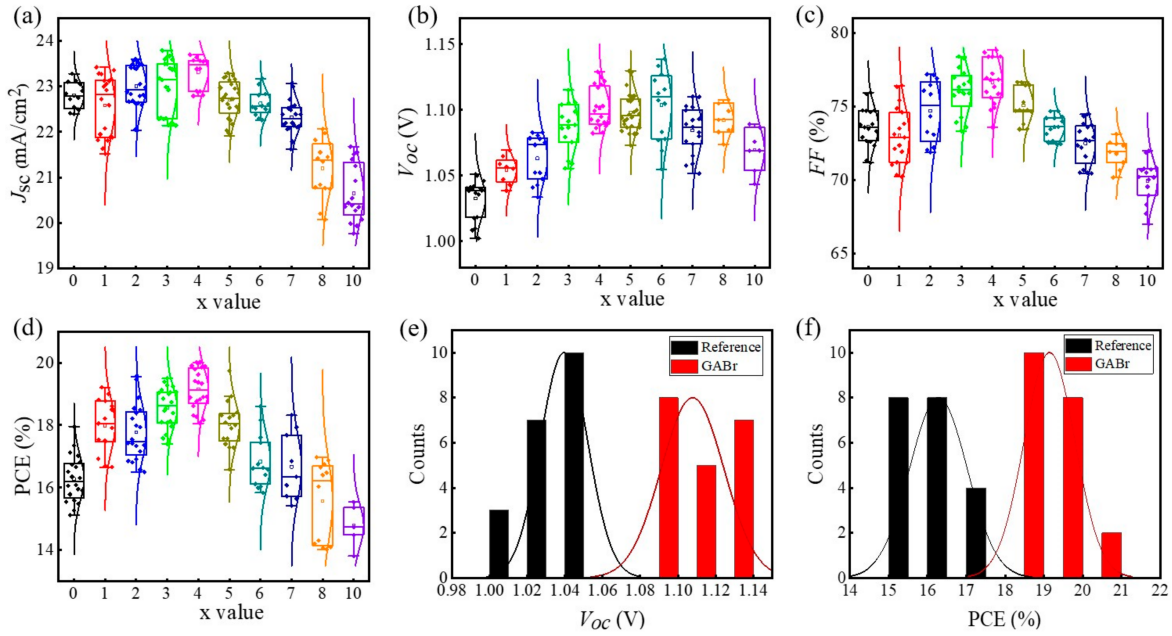

Figure 2. Statistical *J-V* parameters of (**a**) J_{sc}, (**b**) V_{oc}, (**c**) *FF*, and (**d**) PCE of devices modified by different concentrations of GABr. The histogram of (**e**) V_{oc} and (**f**) PCE for reference devices and GABr-treated devices.

Remarkably, the hysteresis effect tends to be mitigated when x < 5, but when x further increases, severe hysteresis is observed again. Hysteresis Index (HI) is one parameter commonly used to evaluate the hysteresis degree, and HI is defined as:

$$HI = (PCE_{RS} - PCE_{FS})/PCE_{RS}, \quad (2)$$

in which the PCE_{RS} is the efficiency measured under reverse scan direction, and PCE_{FS} represents the efficiency measured under forward scan direction [40]. The HI values of different GABr-treated devices are summarized in Table S1 and the *J-V* curves are shown in Figure S1. Obviously, one can find that moderate GABr post-treatment can reduce the HI, but when the concentration of GABr keeps increasing, the hysteresis becomes critical. Actually, hysteresis issue occurs seriously in $MAPbI_3$-based PSCs with n-i-p planar structure is associated with the dipole moment of MA cation [41]. The suppressed hysteresis effect should be affected by the nearly zero dipole moment of GA^+ [25]. Besides, GA^+ tends to form hydrogen bonds with the unsaturated defects center, which can powerfully suppress ion migration and mitigate the hysteresis effect [19].

The surface morphology of perovskite films is shown in Figure 3. One may find that there are some bright particles on the surface of the pristine $MAPbI_3$, which might be indexable to the excess PbI_2 [42,43]. After treatment, these particles disappear and maintain a dense and pinhole-free surface. When the concentration of GABr increases to x = 8 mg·mL^{-1}, we suppose that excess GABr will react with the PbI_2 inside the perovskite

lattice combined with XRD spectra, and then forming a two-dimensional GA_2PbI_4 capping layer with disordered and smaller crystals (as shown in Figure S2). Due to the insulating nature of 2D perovskite, this capping layer is supposed to hinder the carrier transportation and cause performance degradation [30].

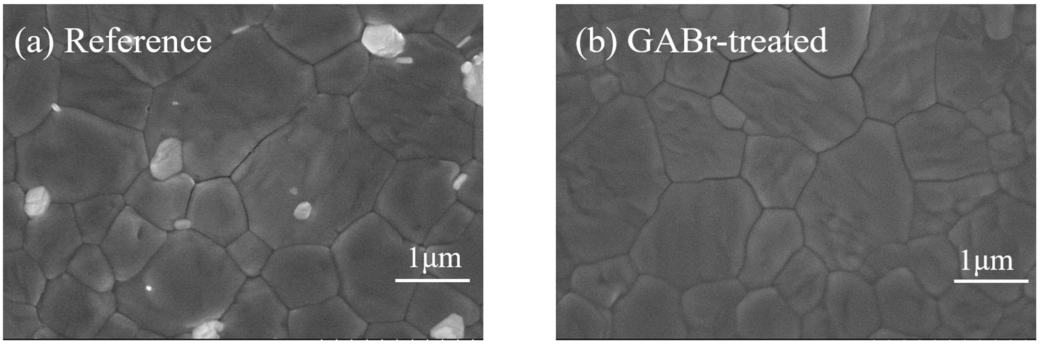

Figure 3. SEM images of (**a**) the reference film, (**b**) GABr-treated $MAPbI_3$.

According to the AFM profile of the pristine and GABr-treated $MAPbI_3$ film shown in Figure 4a,b, GABr-treated film shows RMS = 8.76 nm, which is slightly lower than that of the pristine one (RMS = 12.3 nm), which is consistent with the SEM results. The decreased surface roughness is beneficial for the device performance because it can effectively reduce the contact resistance between perovskite layer and HTL. Moreover, we conduct Kelvin probe force microscopy (KPFM) to observe the surface potential change after GABr treatment as shown in Figure 4c,d. GABr-treated film presents a more uniform surface potential than reference film. It has been demonstrated that the grain boundaries surrounded by grains with large contact potential difference (illustrated as #1 in Figure 4c,d) would induce severe hysteresis in local photocurrents [44]. The decrease in the number of grain boundaries #1 in GABr-treated film suggests that GABr treatment is beneficial to produce superior perovskite with more uniform surface potential and thus forcefully suppress the hysteresis effect.

The influence in chemical component of GABr treatment is investigated by X-ray photoelectron spectroscopy (XPS). Figure 5b–e show the core spectra of I 3d, Pb 4f, N 1s, and C 1s. The spectra of N 1s can be divided into two peaks in GABr-treated samples: the peak at 402.04 eV attributed to NH_3^+ group in MA, and the peak at 400.12 eV to NH_2^+ group in GA [45]. The spectra of I 3d, N 1s and Pb 4f exhibit a slight shift after post-treatment, which indicates that GABr treatment will induce an influence on the chemical environment of these elements. The ratio of each element is listed in Table S2, the Pb/I ratio decreases from 39.3% to 37.5% after GABr treatment, which further confirms the reaction between PbI_2 and GABr.

Furthermore, the work function (W_F) and the valence band (VB) maximum are measured by ultraviolet photoelectron spectroscopy (UPS). Figure 5f shows the secondary electron edge cut-offs (E_{cutoff}) and valence band maximum (E_{VBM}) spectra of pristine and GABr-treated $MAPbI_3$. The E_{cutoff} and E_{VBM} are obtained by the extrapolation of the line fit to the cut-off edge. According to Einstein's photoemission law ($W_F = h\nu - E_{cutoff} - E_F$), W_F is calculated to be 3.837 eV and 3.917 eV, and the E_{VBM} is obtained to be 1.47 eV and 1.45 eV of $MAPbI_3$ and GABr-treated sample [46]. This result reveals that the film treated by GABr is less n-type, and an upward shift of E_{VBM}, which will decrease the charge transport barrier between perovskite and Spiro-OMeTAD. The modified band alignment can make more effective charge separation and collection, which might effectively suppress the charge recombination at the interface and improve the device performance [47,48].

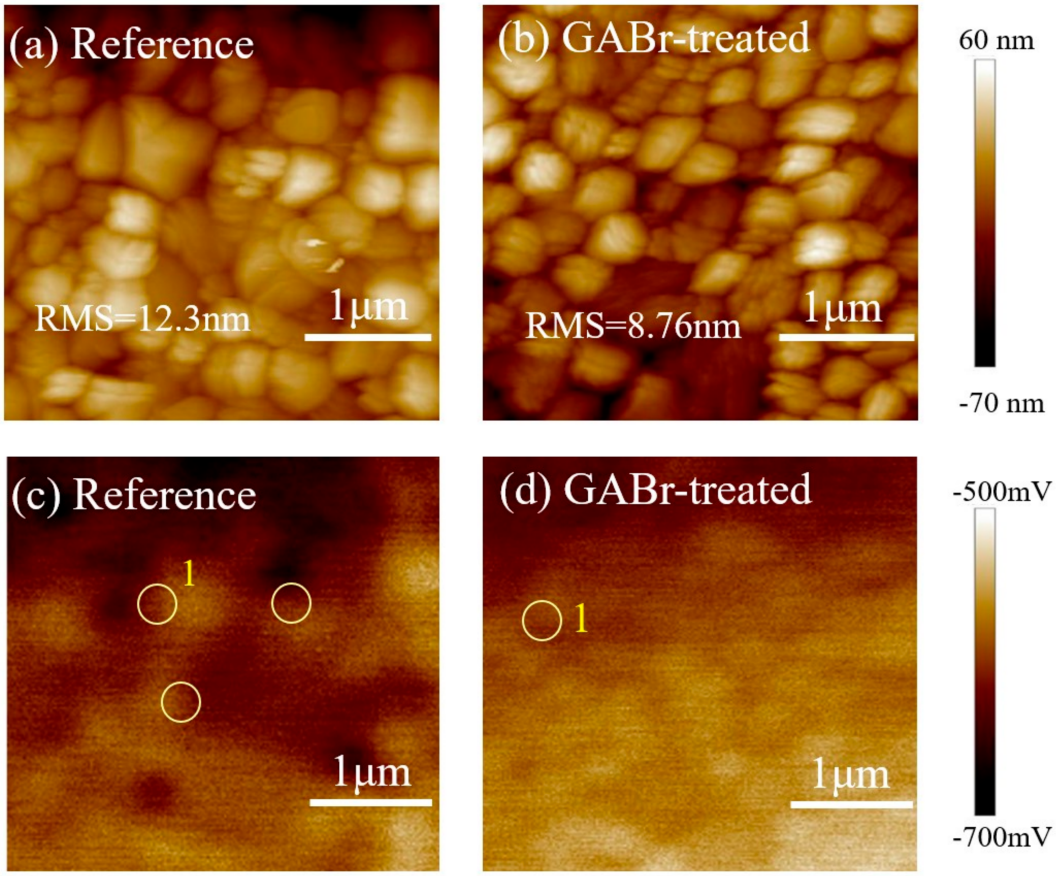

Figure 4. AFM morphology of (**a**) the reference film, (**b**) GABr-treated $MAPbI_3$. KPFM images of (**c**) the reference film and (**d**) GABr-treated $MAPbI_3$. In Figure 4c,d, the yellow circle represents the type of grain boundary #1.

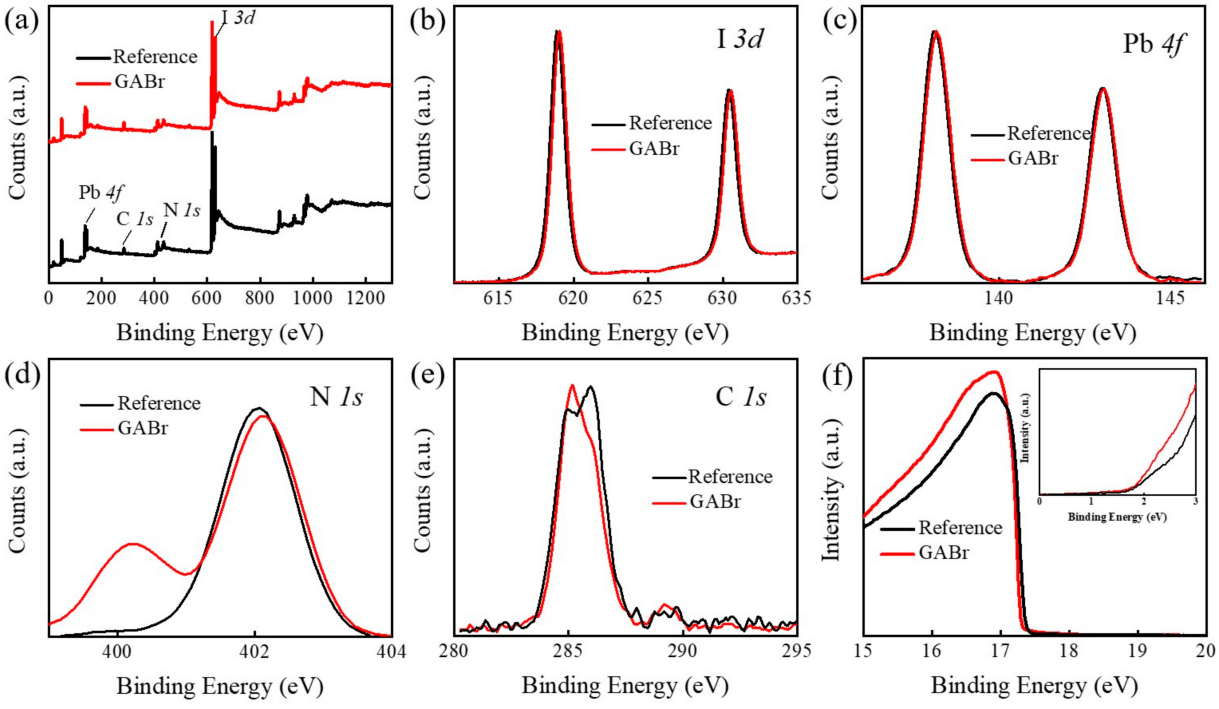

Figure 5. (**a**) The elemental survey spectra of $MAPbI_3$ and GABr-treated $MAPbI_3$. High-resolution XPS spectra of (**b**) I 3d, (**c**) Pb 4f, (**d**) N 1s, (**e**) C 1s of $MAPbI_3$ and GABr-treated $MAPbI_3$. (**f**) The UPS secondary electron edge cut-offs of these two samples, and the inner image is the corresponding magnified details of the valence band spectra.

Afterwards, pristine $MAPbI_3$ and GABr-treated perovskite film are prepared on quartz substrate for steady-state Photoluminescence (PL) and time-resolved PL decay (TRPL) measurement. In Figure 6a, the PL emission peak shifts from 770 nm to 766 nm after GABr treatment, which is in keeping with the absorption spectra. Moreover, the intensity of PL peak of GABr-treated film is much stronger than the pristine film, suggesting a superior film with fewer density of defects and suppressed nonradiative recombination (as shown in Figure 6b) [49–51]. The TRPL curve can be fitted by a biexponential equation [23]:

$$f(t) = A_1 \exp(-t/\tau_1) + A_2 \exp(-t/\tau_2), \quad (3)$$

where τ_1, τ_2 refer to the fast-decay and long-decay recombination mechanism, A_1, A_2 are the corresponding coefficients. The fast decay is related with the rapid charge transfer at interlayer, and the long process is attributed to the bulk and interface recombination [52]. After calculation, GABr-treated $MAPbI_3$ shows both increasement in τ_1 and τ_2 (the fitting results are given in the table inserted in Figure 5c). The average carrier lifetime (τ_{ave}) is estimated according to the following equation [53]:

$$\tau_{ave} = (A_1 \tau_1^2 + A_2 \tau_2^2)/(A_1 \tau_1 + A_2 \tau_2), \quad (4)$$

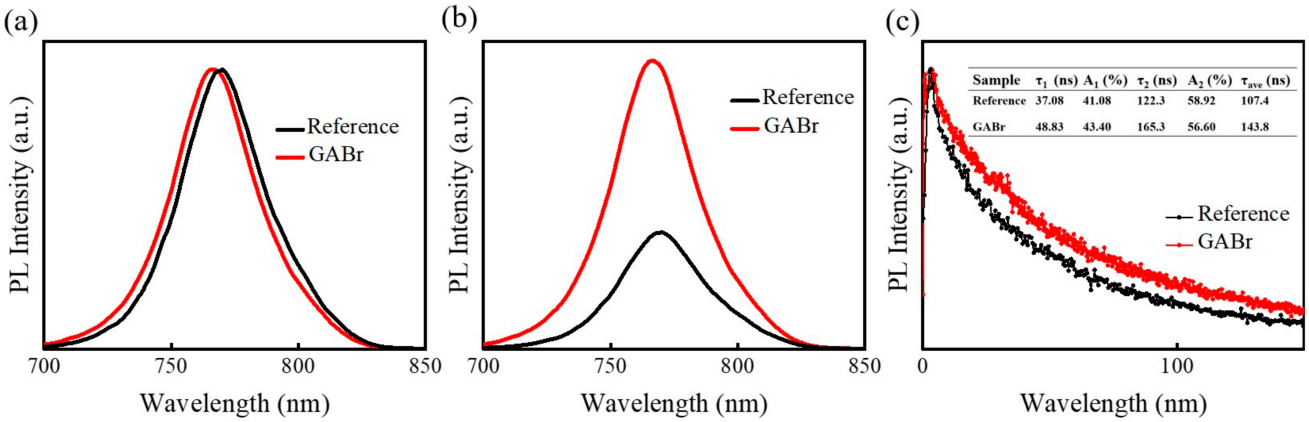

Figure 6. (**a**) The normalized Photoluminescence (PL) spectra of $MAPbI_3$ and GABr-treated film. (**b**) PL and (**c**) time-resolved PL (TRPL) results of $MAPbI_3$ and GABr-treated films, and the inset table is the corresponding parameters of the fitting results.

The τ_{ave}'s are 107.4 ns and 143.8 ns for the reference perovskite and GABr-treated film, respectively. The longer decay time of GABr-treated film further indicates fewer defect states and a suppression of nonradiative recombination [54]. It is well known that GA^+ cation is a Lewis acid with a symmetrical structure, which allows the formation of hydrogen bonds between the partial negative (δ^-) iodine ions and partly positively charged (δ^+) ammonium H atoms [19,55]. Overall, we propose that after post-treatment, GA^+ trends to bond with free iodide ion and thus successfully passivates the nonradiative recombination.

The *J-V* curves of the champion devices are displayed in Figure 7a. The pristine device achieves a best PCE of 17.95% with a V_{oc} of 1.055 V, a J_{sc} of 22.93 mA/cm^2 and an *FF* of 74.21%, and the GABr-treated device shows better performance with overall improvement in V_{oc} (1.13 V) and *FF* (76.81%) while maintaining the performance of J_{sc} (23.06 mA/cm^2). The *J-V* parameters of devices measured under different scan directions are summarized in Table S3. Figure 7b shows the external quantum efficiency (EQE) spectra of the champion performance devices. The integrated J_{sc}'s are 21.49 mA/cm^2 for reference device and 21.63 mA/cm^2 for the GABr-treated device, which is consistent with *J-V* measurement result.

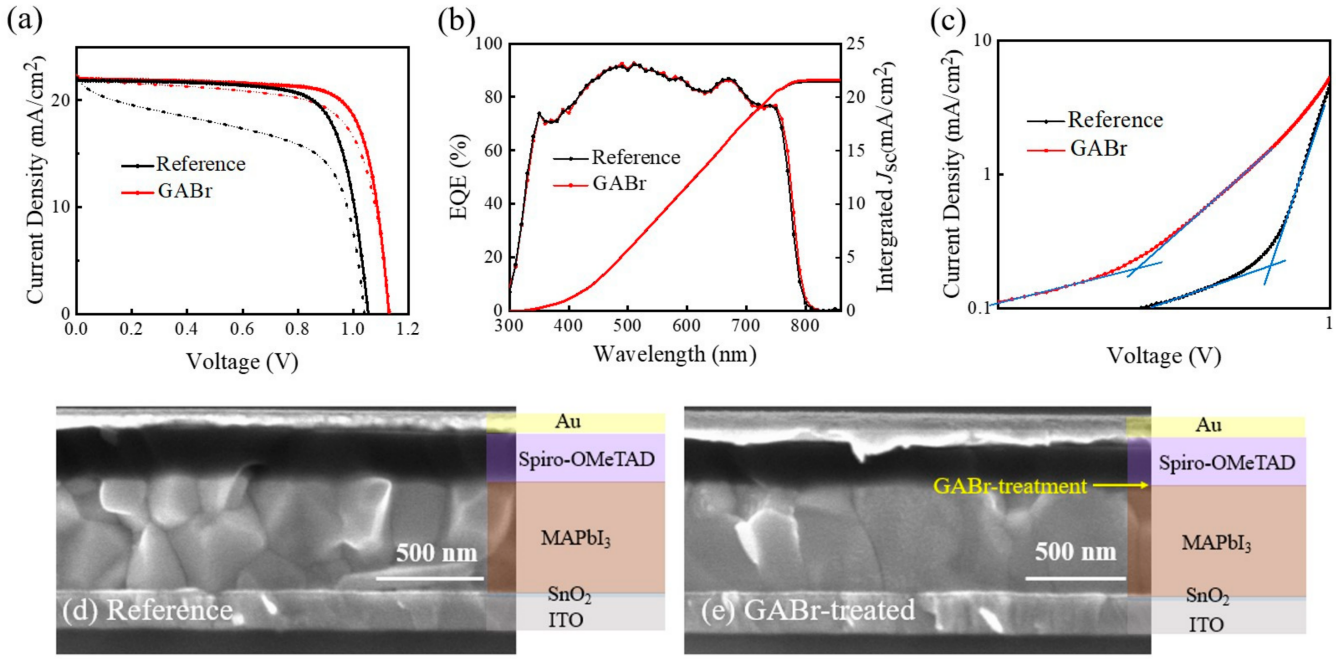

Figure 7. (**a**) The *J-V* curves, (**b**) external quantum efficiency (EQE) spectra and (**c**) space-charge-limited current (SCLC) results of the champion devices based on $MAPbI_3$ and GABr-treated device. The cross-sectional SEM images of (**d**) reference devices, and (**e**) GABr-based devices.

To further understand the passivation effect of GABr, a space-charge-limited current (SCLC) measurement is conducted to calculate the density of defect. Then, we prepare devices with structure of ITO/PEDOT:PSS/PVSK/Spiro-OMeTAD/Au to investigate the trap-state density (n_{trap}). The n_{trap} can be obtained according to equation [23]:

$$n_{trap} = 2\varepsilon\varepsilon_0 V_{TFL}/qL^2, \quad (5)$$

where ε is the relative dielectric constant of the perovskite material, ε_0 is the vacuum permittivity, L is the thickness of perovskite layer, q is the electron charge and V_{TFL} is the trap-filled limit voltage [56,57]. The calculated n_{trap}'s are 8.1×10^{15} cm^{-3} and 2.04×10^{16} cm^{-3} for GABr-treated $MAPbI_3$ and pristine $MAPbI_3$, respectively. The decreased trap-state density after GABr treatment means lower charge recombination rate and improved film quality, which might lead to higher V_{oc} and *FF* of device [53,58,59].

Devices with a structure of ITO/SnO_2/$MAPbI_3$/Spiro-OMeTAD/Au are made for cross-sectional SEM characterization. As shown in Figure 7d,e, compared with the reference perovskite layer composed of grains with various sizes, GABr-treated film displays fewer grain boundaries and more uniform grain size. The interface between $MAPbI_3$ and Spiro-OMeTAD is more uniform after GABr treatment, which suggests a lower contact resistance. The reduction of grain boundaries should be helpful to suppress the ion diffusion between the perovskite layer and transport layer of the devices [60]. Meanwhile, GABr-treated perovskite performs almost vertical grain boundaries, which attesting the decreasing of carrier trap interface and photocurrent conduction pathway [61].

Moreover, we monitor the stability performance of reference and GABr-treated devices (shown in Figure 8). GABr-treated device shows a steady-state PCE of 19.95% in a duration of 300 s, while untreated device experiences serious decay. The poor steady-state PCE of untreated device should be resulted from the aggravated ion migration due to the increased temperature under continuous illumination, and serious nonradiative recombination induced by defects [5,62]. The long-term stability is also recorded (the devices are stored and tested in a N_2-filled glove box) and the GABr modified device can retain over 90% of its original PCE after 30 days. On the contrary, the efficiency of the controlled one rapidly degraded to 90% of the initial value in merely 10 days. The main reason of the optimized

stability for GABr treated devices is the improved crystallinity with decreased defect states of the perovskite layer, which enhances its resistance to moisture, oxygen and/or light irradiation [27,55].

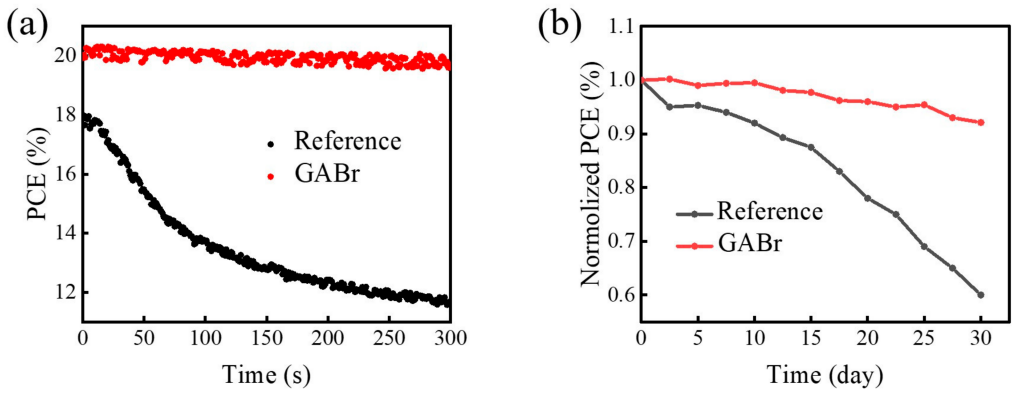

Figure 8. (**a**) Steady-state power conversion efficiency (PCE) of the champion devices with/without treatment, (**b**) Long-term stability trace of champion devices stored and tested in N_2-filled glove box after 30 days.

Thus, we have proved that GABr treatment can result in a substantial improvement in the performance of $MAPbI_3$ PSCs fabricated on rigid glass. Then we attempt to verify the effect of GABr treatment on flexible devices. The XRD and SEM spectra of perovskite with/without GABr treatment are shown in Figures S3 and S4. Interestingly, the perovskite films show preferred orientation. After modification, the continuity of the film is improved while the grain boundary gets blurred. The unusual crystal orientation and surface morphology should be caused by the special properties of the underneath substrates.

The *J-V* curve and EQE spectra of the champion devices based on $MAPbI_3$ and GABr-treated perovskite are shown in Figure 9a,b. On a flexible substrate, GABr-devices still exhibit a significant enhancement in V_{oc} with slight improved J_{sc} and *FF* and achieve a best PCE of 17.57%. The integrated J_{sc}'sare 19.93 mA/cm^2 and 20.34 mA/cm^2 of pristine and GABr-treated device, respectively. Compared with rigid devices, the EQE response in wavelength region of 300–400 nm is suppressed in flexible devices due to the strong absorption of PEN-ITO in this region (the transmittance spectra of the two substrates are shown in Figure S5). HI index values and *J-V* parameters are listed on Table S4. The HI effect is also being reduced after GABr treatment. The PL and TRPL spectra of flexible samples are shown in Figure 9c–e. The tendency is consistent with the samples deposited on rigid substrates. The carrier lifetime is prolonged to 139.85 ns after post-treatment, while the lifetime of pristine film is 111.54 ns.

The main issues of the performance of flexible devices are the low *FF* due to the high series resistance (R_s), and the worse J_{sc} affected by the surface properties the flexible substrate [63]. R_s of the controlled and GABr-treated devices deposited on different substrates is summarized in Figure 9f. This result indicates that GABr post-treatment can effectively reduce the R_s of the devices, which can be attributed to the modified surface morphology of perovskite layer [33]. The obstacles in the development of flexible PSCs based on PEN-ITO or PET-ITO are the worse efficiency, brittleness of ITO and the relatively high cost. It still needs more efforts to exploit cheaper conductive electrode materials with better bending resistance and transparency and employ effective strategies to boost the application.

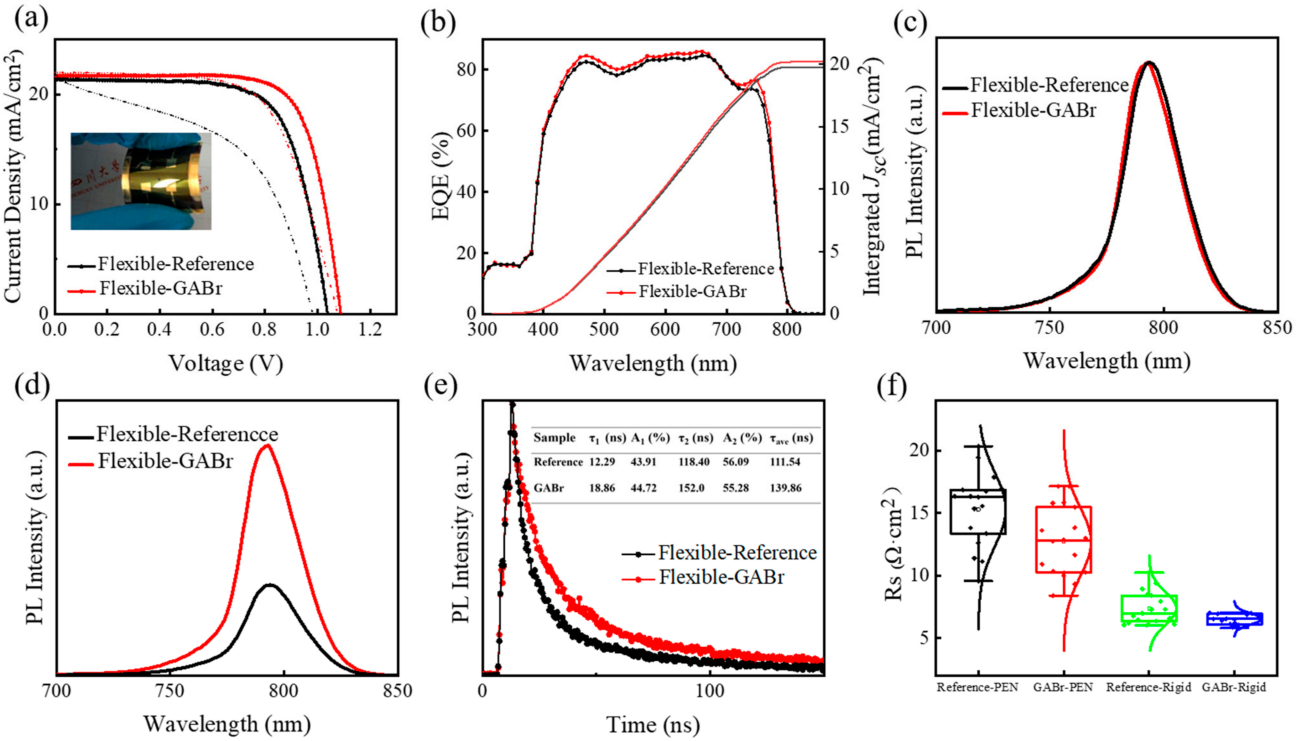

Figure 9. (**a**) The *J-V* curves and (**b**) EQE spectra of the champion cells based on $MAPbI_3$ and GABr-treated flexible device. (**c**) The normalized PL spectra of $MAPbI_3$ and GABr-treated film. (**d**) PL and (**e**) TRPL results of $MAPbI_3$ and GABr-treated films, and the inset table is the corresponding parameters of the fitting results. (**f**) The statistical results of R_s of pristine devices and GABr-based devices deposited on two substrates.

4. Conclusions

In conclusion, we propose a simple GABr-post treatment to enhance the crystallinity of $MAPbI_3$, increase the carrier lifetime, and boost the PCE to over 20% on rigid substrate. The average V_{oc} is increased by 80 mV and the serious hysteresis in $MAPbI_3$-based planar devices is significantly eliminated after GABr treatment. The application of GABr leads to a better band energy matching between perovskite and spiro-OMeTAD, which is beneficial for charge transport. In addition, the treatment results in a superior $MAPbI_3$ film and can effectively passivate the trap states. This work also demonstrates that GABr treatment is a feasible approach to improve the efficiency of $MAPbI_3$ solar cells fabricated on flexible PEN substrate. Thanks to the eliminated V_{oc} loss after GABr treatment, the PCE of flexible devices increases from 15.77% to over 17.57%.

Supplementary Materials: The following are available online at https://www.mdpi.com/2079-4991/11/3/750/s1, Figure S1: *J-V* curves of devices treated by high concentration of GABr measured under different scan directions, Figure S2: (a) SEM image of 8 mg·mL^{-1} GABr treated $MAPbI_3$ and (b) the cross-sectional SEM image of 8 mg·mL^{-1} GABr treated solar cell device, Figure S3: XRD spectra of $MAPbI_3$ and GABr treated $MAPbI_3$ deposited on flexible substrates, Figure S4: SEM images of (a) $MAPbI_3$ and (b) GABr treated $MAPbI_3$ deposited on flexible substrates, Figure S5: The transmittance spectra for both substrates for rigid and flexible devices, Table S1:HI values of devices treated by different concentrations of GABr, Table S2: Atomic ratio of $MAPbI_3$ and GABr-treated film obtained from XPS data, Table S3: *J-V* parameters of the champion devices based on $MAPbI_3$ and GABr-treated $MAPbI_3$ on rigid substrates, Table S4: *J-V* parameters and HI values of the champion devices based on $MAPbI_3$ and GABr-treated $MAPbI_3$ on flexible substrates.

Author Contributions: Conceptualization, T.C., R.H., X.H., D.Z. and J.Z. Software, T.C., R.H. and W.W. Investigation, T.C., R.H., F.Z., Z.X. and Y.W. Writing—original draft preparation, T.C., R.H. Writing—review and editing, X.H., L.W. Funding acquisition, X.H., L.W., D.Z., and J.Z. All authors have read and agreed to the published version of the manuscript.

Funding: This work was funded by the Science and Technology Program of Sichuan Province (Nos. 2021YFG0102, 2019ZDZX0015, 2020YFH0079 and 2020JDJQ0030), the Fundamental Research Funds for the Central Universities (Nos. YJ201722 and YJ201955).

Data Availability Statement: The data presented in this study are available on request from the corresponding author.

Acknowledgments: We would like to thank Yingming Zhu from the Institute of New Energy and Low-Carbon Technology, Sichuan University, for his help of SEM images capturing and analysis work.

Conflicts of Interest: The authors declare no conflict of interest.

References

1. Green, M.A.; Jiang, Y.; Soufiani, A.M.; Ho-Baillie, A. Optical Properties of Photovoltaic Organic-Inorganic Lead Halide Perovskites. *J. Phys. Chem. Lett.* **2015**, *6*, 4774–4785. [CrossRef]
2. Miyata, A.; Mitioglu, A.; Plochocka, P.; Portugall, O.; Wang, J.T.-W.; Stranks, S.D.; Snaith, H.J.; Nicholas, R.J. Direct measurement of the exciton binding energy and effective masses for charge carriers in organic-inorganic trihalide perovskites. *Nat. Phys.* **2015**, *11*, 582–587. [CrossRef]
3. Stranks, S.D.; Eperon, G.E.; Grancini, G.; Menelaou, C.; Alcocer, M.J.; Leijtens, T.; Herz, L.M.; Petrozza, A.; Snaith, H.J. Electron-hole diffusion lengths exceeding 1 micrometer in an organometal trihalide perovskite absorber. *Science* **2013**, *342*, 341–344. [CrossRef]
4. Best Performance-NREL. Available online: https://www.nrel.gov/pv/cell-efficiency.html (accessed on 4 January 2021).
5. Fu, Q.; Tang, X.; Huang, B.; Hu, T.; Tan, L.; Chen, L.; Chen, Y. Recent Progress on the Long-Term Stability of Perovskite Solar Cells. *Adv. Sci.* **2018**, *5*, 1700387. [CrossRef] [PubMed]
6. Tao, H.; Wang, J.; Zhang, C.; Zhang, W.; Tan, B.; Li, Y.; Han, L.; Tao, J. Improving the efficiency of degenerated perovskite solar cells by a simple freeze treatment. *Mater. Sci. Semicond. Process.* **2019**, *93*, 260–265. [CrossRef]
7. De Wolf, S.; Holovsky, J.; Moon, S.J.; Loper, P.; Niesen, B.; Ledinsky, M.; Haug, F.J.; Yum, J.H.; Ballif, C. Organometallic Halide Perovskites: Sharp Optical Absorption Edge and Its Relation to Photovoltaic Performance. *J. Phys. Chem. Lett.* **2014**, *5*, 1035–1039. [CrossRef] [PubMed]
8. Li, P.S.; Balamurugan, R.; Liu, B.T.; Lee, R.H.; Chou, H.T. MAPbI3 Incorporated with Carboxyl Group Chelated Titania for Planar Perovskite Solar Cells in Low-Temperature Process. *Nanomaterials* **2019**, *9*, 908. [CrossRef]
9. Zou, Y.; Wang, H.-Y.; Qin, Y.; Mu, C.; Li, Q.; Xu, D.; Zhang, J.-P. Reduced Defects of $MAPbI_3$ Thin Films Treated by FAI for High-Performance Planar Perovskite Solar Cells. *Adv. Funct. Mater.* **2019**, *29*, 1805810. [CrossRef]
10. Ball, J.M.; Petrozza, A. Defects in perovskite-halides and their effects in solar cells. *Nat. Energy* **2016**, *1*, 16149. [CrossRef]
11. Choi, J.J.; Yang, X.; Norman, Z.M.; Billinge, S.J.L.; Owen, J.S. Structure of Methylammonium Lead Iodide within Mesoporous Titanium Dioxide: Active Material in High-Performance Perovskite Solar Cells. *Nano Lett.* **2013**, *14*, 127–133. [CrossRef]
12. Manser, J.S.; Saidaminov, M.I.; Christians, J.A.; Bakr, O.M.; Kamat, P.V. Making and Breaking of Lead Halide Perovskites. *Acc. Chem. Res.* **2016**, *49*, 330–338. [CrossRef]
13. Konidakis, I.; Maksudov, T.; Serpetzoglou, E.; Kakavelakis, G.; Kymakis, E.; Stratakis, E. Improved Charge Carrier Dynamics of CH3NH3PbI3 Perovskite Films Synthesized by Means of Laser-Assisted Crystallization. *ACS Appl. Energy Mater.* **2018**, *1*, 5101–5111. [CrossRef]
14. Iftiquar, S.M.; Yi, J. Impact of grain boundary defect on performance of perovskite solar cell. *Mater. Sci. Semicond. Process.* **2018**, *79*, 46–52. [CrossRef]
15. Wang, C.; Xiao, C.; Yu, Y.; Zhao, D.; Awni, R.A.; Grice, C.R.; Ghimire, K.; Constantinou, I.; Liao, W.; Cimaroli, A.J.; et al. Understanding and Eliminating Hysteresis for Highly Efficient Planar Perovskite Solar Cells. *Adv. Energy Mater.* **2017**, *7*, 1700414. [CrossRef]
16. Yuan, Y.; Wang, Q.; Shao, Y.; Lu, H.; Li, T.; Gruverman, A.; Huang, J. Electric-Field-Driven Reversible Conversion Between Methylammonium Lead Triiodide Perovskites and Lead Iodide at Elevated Temperatures. *Adv. Energy Mater.* **2016**, *6*, 1501803. [CrossRef]
17. Li, W.; Thirumurugan, A.; Barton, P.T.; Lin, Z.; Henke, S.; Yeung, H.H.; Wharmby, M.T.; Bithell, E.G.; Howard, C.J.; Cheetham, A.K. Mechanical tunability via hydrogen bonding in metal-organic frameworks with the perovskite architecture. *J. Am. Chem. Soc.* **2014**, *136*, 7801–7804. [CrossRef] [PubMed]
18. Jeanbourquin, X.A.; Li, X.; Law, C.; Barnes, P.R.; Humphry-Baker, R.; Lund, P.; Asghar, M.I.; O'Regan, B.C. Rediscovering a key interface in dye-sensitized solar cells: Guanidinium and iodine competition for binding sites at the dye/electrolyte surface. *J. Am. Chem. Soc.* **2014**, *136*, 7286–7294. [CrossRef]
19. De Marco, N.; Zhou, H.; Chen, Q.; Sun, P.; Liu, Z.; Meng, L.; Yao, E.P.; Liu, Y.; Schiffer, A.; Yang, Y. Guanidinium: A Route to Enhanced Carrier Lifetime and Open-Circuit Voltage in Hybrid Perovskite Solar Cells. *Nano Lett.* **2016**, *16*, 1009–1016. [CrossRef]
20. Zhou, X.; Zhang, L.; Wang, X.; Liu, C.; Chen, S.; Zhang, M.; Li, X.; Yi, W.; Xu, B. Highly Efficient and Stable GABr-Modified Ideal-Bandgap (1.35 eV) Sn/Pb Perovskite Solar Cells Achieve 20.63% Efficiency with a Record Small Voc Deficit of 0.33 V. *Adv. Mater.* **2020**, *32*, 1908107. [CrossRef]

21. Yan, C.; Li, Z.; Sun, Y.; Zhao, J.; Huang, X.; Yang, J.; Ci, Z.; Ding, L.; Jin, Z. Decreasing energy loss and optimizing band alignment for high performance CsPbI3 solar cells through guanidine hydrobromide post-treatment. *J. Mater. Chem. A* **2020**, *8*, 10346–10353. [CrossRef]
22. Chen, C.; Song, Z.; Xiao, C.; Zhao, D.; Shrestha, N.; Li, C.; Yang, G.; Yao, F.; Zheng, X.; Ellingson, R.J.; et al. Achieving a high open-circuit voltage in inverted wide-bandgap perovskite solar cells with a graded perovskite homojunction. *Nano Energy* **2019**, *61*, 141–147. [CrossRef]
23. Zhang, W.; Xiong, J.; Li, J.; Daoud, W.A. Guanidinium Passivation for Air-Stable Rubidium-Incorporated $Cs_{(1-x)}Rb_xPbI_2Br$ Inorganic Perovskite Solar Cells. *Sol. RRL* **2020**, *4*, 2000112. [CrossRef]
24. Liu, P.; Wang, W.; Liu, S.; Yang, H.; Shao, Z. Fundamental Understanding of Photocurrent Hysteresis in Perovskite Solar Cells. *Adv. Energy Mater.* **2019**, *9*, 1803017. [CrossRef]
25. Giorgi, G.; Yamashita, K. Zero-dipole molecular organic cations in mixed organic–inorganic halide perovskites: Possible chemical solution for the reported anomalous hysteresis in the current-voltage curve measurements. *Nanotechnology* **2015**, *26*, 442001. [CrossRef]
26. Giorgi, G.; Fujisawa, J.-I.; Segawa, H.; Yamashita, K. Organic-Inorganic Hybrid Lead Iodide Perovskite Featuring Zero Dipole Moment Guanidinium Cations: A Theoretical Analysis. *J. Phys. Chem. C* **2015**, *119*, 4694–4701. [CrossRef]
27. Xu, Z.; Chen, R.; Wu, Y.; He, R.; Yin, J.; Lin, W.; Wu, B.; Li, J.; Zheng, N. Br-containing alkyl ammonium salt-enabled scalable fabrication of high-quality perovskite films for efficient and stable perovskite modules. *J. Mater. Chem. A* **2019**, *7*, 26849–26857. [CrossRef]
28. Kim, D.; Jung, H.J.; Park, I.J.; Larson, B.W.; Dunfield, S.P.; Xiao, C.; Kim, J.; Tong, J.; Boonmongkolras, P.; Ji, S.G.; et al. Efficient, stable silicon tandem cells enabled by anion-engineered wide-bandgap perovskites. *Science* **2020**, *368*, 155–160. [CrossRef]
29. Kim, D.H.; Muzzillo, C.P.; Tong, J.; Palmstrom, A.F.; Larson, B.W.; Choi, C.; Harvey, S.P.; Glynn, S.; Whitaker, J.B.; Zhang, F.; et al. Bimolecular Additives Improve Wide-Band-Gap Perovskites for Efficient Tandem Solar Cells with CIGS. *Joule* **2019**, *3*, 1734–1745. [CrossRef]
30. Wei, M.; Xiao, K.; Walters, G.; Lin, R.; Zhao, Y.; Saidaminov, M.I.; Todorovic, P.; Johnston, A.; Huang, Z.; Chen, H.; et al. Combining Efficiency and Stability in Mixed Tin-Lead Perovskite Solar Cells by Capping Grains with an Ultrathin 2D Layer. *Adv. Mater.* **2020**, *32*, e1907058. [CrossRef]
31. Xiong, S.; Hou, Z.; Zou, S.; Lu, X.; Yang, J.; Hao, T.; Zhou, Z.; Xu, J.; Zeng, Y.; Xiao, W.; et al. Direct Observation on p- to n-Type Transformation of Perovskite Surface Region during Defect Passivation Driving High Photovoltaic Efficiency. *Joule* **2021**, *5*, 1–14. [CrossRef]
32. Chen, C.; Jiang, Y.; Guo, J.; Wu, X.; Zhang, W.; Wu, S.; Gao, X.; Hu, X.; Wang, Q.; Zhou, G.; et al. Solvent-Assisted Low-Temperature Crystallization of SnO_2 Electron-Transfer Layer for High-Efficiency Planar Perovskite Solar Cells. *Adv. Funct. Mater.* **2019**, *29*, 1900557. [CrossRef]
33. Lim, J.W.; Wang, H.; Choi, C.H.; Quan, L.N.; Chung, K.; Park, W.-T.; Noh, Y.-Y.; Kim, D.H. Polyethylenimine ethoxylated interlayer-mediated ZnO interfacial engineering for high-performance and low-temperature processed flexible perovskite solar cells: A simple and viable route for one-step processed CH3NH3PbI3. *J. Power Sources* **2019**, *438*, 226956. [CrossRef]
34. Kumar, G.S.; Sarkar, P.K.; Pradhan, B.; Hossain, M.; Rao, K.D.M.; Acharya, S. Large-area transparent flexible guanidinium incorporated MAPbI3 microstructures for high-performance photodetectors with enhanced stability. *Nanoscale Horiz.* **2020**, *5*, 696–704. [CrossRef]
35. Luo, D.; Yang, W.; Wang, Z.; Sadhanala, A.; Hu, Q.; Su, R.; Shivanna, R.; Trindade, G.F.; Watts, J.F.; Xu, Z.; et al. Enhanced photovoltage for inverted planar heterojunction perovskite solar cells. *Science* **2018**, *360*, 1442–1446. [CrossRef] [PubMed]
36. Zheng, Y.; Yang, X.; Su, R.; Wu, P.; Gong, Q.; Zhu, R. High-Performance $CsPbI_xBr_{3-x}$ All-Inorganic Perovskite Solar Cells with Efficiency over 18% via Spontaneous Interfacial Manipulation. *Adv. Funct. Mater.* **2020**, *30*, 2000457. [CrossRef]
37. Vega, E.; Mollar, M.; Marí, B. Effect of guanidinium on the optical properties and structure of the methylammonium lead halide perovskite. *J. Alloy. Compd.* **2018**, *739*, 1059–1064. [CrossRef]
38. Zheng, D.; Tong, C.; Zhu, T.; Rong, Y.; Pauporte, T. Effects of 5-Ammonium Valeric Acid Iodide as Additive on Methyl Ammonium Lead Iodide Perovskite Solar Cells. *Nanomaterials* **2020**, *10*, 2512. [CrossRef] [PubMed]
39. Jodlowski, A.D.; Yépez, A.; Luque, R.; Camacho, L.; de Miguel, G. Benign-by-Design Solventless Mechanochemical Synthesis of Three-, Two-, and One-Dimensional Hybrid Perovskites. *Angew. Chem. Int. Ed.* **2016**, *128*, 15196–15201. [CrossRef]
40. Li, Z.; Tinkham, J.; Schulz, P.; Yang, M.; Kim, D.H.; Berry, J.; Sellinger, A.; Zhu, K. Acid Additives Enhancing the Conductivity of Spiro-OMeTAD Toward High-Efficiency and Hysteresis-Less Planar Perovskite Solar Cells. *Adv. Energy Mater.* **2017**, *7*, 1601451. [CrossRef]
41. Lee, J.W.; Seol, D.J.; Cho, A.N.; Park, N.G. High-efficiency perovskite solar cells based on the black polymorph of HC(NH2)2 PbI3. *Adv. Mater.* **2014**, *26*, 4991–4998. [CrossRef] [PubMed]
42. Yu, Y.; Wang, C.; Grice, C.R.; Shrestha, N.; Zhao, D.; Liao, W.; Guan, L.; Awni, R.A.; Meng, W.; Cimaroli, A.J.; et al. Synergistic Effects of Lead Thiocyanate Additive and Solvent Annealing on the Performance of Wide-Bandgap Perovskite Solar Cells. *ACS Energy Lett.* **2017**, *2*, 1177–1182. [CrossRef]
43. Sun, K.; Chang, J.; Isikgor, F.H.; Li, P.; Ouyang, J. Efficiency enhancement of planar perovskite solar cells by adding zwitterion/LiF double interlayers for electron collection. *Nanoscale* **2015**, *7*, 896–900. [CrossRef] [PubMed]

44. Shao, Y.; Fang, Y.; Li, T.; Wang, Q.; Dong, Q.; Deng, Y.; Yuan, Y.; Wei, H.; Wang, M.; Gruverman, A.; et al. Grain boundary dominated ion migration in polycrystalline organic–inorganic halide perovskite films. *Energ. Environ. Sci.* **2016**, *9*, 1752–1759. [CrossRef]
45. Jodlowski, A.D.; Roldán-Carmona, C.; Grancini, G.; Salado, M.; Ralaiarisoa, M.; Ahmad, S.; Koch, N.; Camacho, L.; de Miguel, G.; Nazeeruddin, M.K. Large guanidinium cation mixed with methylammonium in lead iodide perovskites for 19% efficient solar cells. *Nat. Energy* **2017**, *2*, 972–979. [CrossRef]
46. Ren, S.; Li, H.; Lei, C.; Li, C.; Yin, X.; Wu, L.; Li, W.; Zhang, J.; Wang, W.; Feng, L. Interface modification to enhance electron extraction by deposition of a ZnMgO buffer on SnO2-coated FTO in CdTe solar cells. *Sol. Energy* **2019**, *177*, 545–552. [CrossRef]
47. Ru, P.; Bi, E.; Zhang, Y.; Wang, Y.; Kong, W.; Sha, Y.; Tang, W.; Zhang, P.; Wu, Y.; Chen, W.; et al. High Electron Affinity Enables Fast Hole Extraction for Efficient Flexible Inverted Perovskite Solar Cells. *Adv. Energy Mater.* **2020**, *10*, 1903487. [CrossRef]
48. Liu, C.; Li, W.; Chen, J.; Fan, J.; Mai, Y.; Schropp, R.E.I. Ultra-thin MoOx as cathode buffer layer for the improvement of all-inorganic CsPbIBr2 perovskite solar cells. *Nano Energy* **2017**, *41*, 75–83. [CrossRef]
49. Mateen, M.; Arain, Z.; Liu, X.; Iqbal, A.; Ren, Y.; Zhang, X.; Liu, C.; Chen, Q.; Ma, S.; Ding, Y.; et al. Boosting optoelectronic performance of MAPbI3 perovskite solar cells via ethylammonium chloride additive engineering. *Sci. China Mater.* **2020**, *63*, 2477–2486. [CrossRef]
50. Yang, L.; Han, G.; Chang, Y.; Zhang, Y.; Xiao, Y. Enhanced efficiency and stability of perovskite solar cells by synergistic effect of magnesium acetate introducing into CH3NH3PbI3. *Mater. Sci. Semicond. Process.* **2019**, *104*, 104671. [CrossRef]
51. Galatopoulos, F.; Papadas, I.T.; Ioakeimidis, A.; Eleftheriou, P.; Choulis, S.A. Surface Treatment of Cu:NiOx Hole-Transporting Layer Using Beta-Alanine for Hysteresis-Free and Thermally Stable Inverted Perovskite Solar Cells. *Nanomaterials* **2020**, *10*, 1961. [CrossRef]
52. Ren, A.; Lai, H.; Hao, X.; Tang, Z.; Xu, H.; Yu Jeco, B.M.F.; Watanabe, K.; Wu, L.; Zhang, J.; Sugiyama, M.; et al. Efficient Perovskite Solar Modules with Minimized Nonradiative Recombination and Local Carrier Transport Losses. *Joule* **2020**, *4*, 1263–1277. [CrossRef]
53. Chen, J.; Xu, J.; Zhao, C.; Zhang, B.; Liu, X.; Dai, S.; Yao, J. Efficient Planar Heterojunction FA1–xCsxPbI3 Perovskite Solar Cells with Suppressed Carrier Recombination and Enhanced Open Circuit Voltage via Anion-Exchange Process. *ACS Appl. Mater. Interfaces* **2019**, *11*, 4597–4606. [CrossRef] [PubMed]
54. Liu, Z.; Deng, K.; Hu, J.; Li, L. Coagulated SnO2 Colloids for High-Performance Planar Perovskite Solar Cells with Negligible Hysteresis and Improved Stability. *Angew. Chem.* **2019**, *58*, 11497–11504. [CrossRef] [PubMed]
55. Pham, N.D.; Tiong, V.T.; Yao, D.; Martens, W.; Guerrero, A.; Bisquert, J.; Wang, H. Guanidinium thiocyanate selective Ostwald ripening induced large grain for high performance perovskite solar cells. *Nano Energy* **2017**, *41*, 476–487. [CrossRef]
56. Zhang, W.; Xiong, J.; Li, J.; Daoud, W.A. Guanidinium induced phase separated perovskite layer for efficient and highly stable solar cells. *J. Mater. Chem. A* **2019**, *7*, 9486–9496. [CrossRef]
57. Wang, Y.; Xiang, P.; Ren, A.; Lai, H.; Zhang, Z.; Xuan, Z.; Wan, Z.; Zhang, J.; Hao, X.; Wu, L.; et al. MXene-Modulated Electrode/SnO2 Interface Boosting Charge Transport in Perovskite Solar Cells. *ACS Appl. Mater. Interfaces* **2020**, *12*, 53973–53983. [CrossRef] [PubMed]
58. Mateen, M.; Arain, Z.; Liu, X.; Liu, C.; Yang, Y.; Ding, Y.; Ma, S.; Ren, Y.; Wu, Y.; Tao, Y.; et al. High-performance mixed-cation mixed-halide perovskite solar cells enabled by a facile intermediate engineering technique. *J. Power Sources* **2020**, *448*, 227386. [CrossRef]
59. He, Z.; Zhang, C.; Meng, R.; Luo, X.; Chen, M.; Lu, H.; Yang, Y. Influence of Ag@SiO2 with Different Shell Thickness on Photoelectric Properties of Hole-Conductor-Free Perovskite Solar Cells. *Nanomaterials* **2020**, *10*, 2364. [CrossRef]
60. Yang, Y.; Wu, L.; Hao, X.; Tang, Z.; Lai, H.; Zhang, J.; Wang, W.; Feng, L. Beneficial effects of potassium iodide incorporation on grain boundaries and interfaces of perovskite solar cells. *RSC Adv.* **2019**, *9*, 28561–28568. [CrossRef]
61. Li, J.J.; Ma, J.Y.; Ge, Q.Q.; Hu, J.S.; Wang, D.; Wan, L.J. Microscopic Investigation of Grain Boundaries in Organolead Halide Perovskite Solar Cells. *ACS Appl. Mater. Interfaces* **2015**, *7*, 28518–28523. [CrossRef]
62. Cho, Y.; Soufiani, A.M.; Yun, J.S.; Kim, J.; Lee, D.S.; Seidel, J.; Deng, X.; Green, M.A.; Huang, S.; Ho-Baillie, A.W.Y. Mixed 3D-2D Passivation Treatment for Mixed-Cation Lead Mixed-Halide Perovskite Solar Cells for Higher Efficiency and Better Stability. *Adv. Energy Mater.* **2018**, *8*, 1703392. [CrossRef]
63. Zhang, J.; Zhang, W.; Cheng, H.-M.; Silva, S.R.P. Critical review of recent progress of flexible perovskite solar cells. *Mater. Today* **2020**, *39*, 66–88. [CrossRef]